

Assessment of Data Consistency through Cascades of Independently Recurrent Inference Machines for fast and robust accelerated MRI reconstruction

D. Karkalousos¹, S. Noteboom², H. E. Hulst^{2,3}, F.M. Vos⁴, M.W.A. Caan¹

¹ Department of Biomedical Engineering & Physics, Amsterdam UMC, University of Amsterdam, Amsterdam, Netherlands

² Department of Anatomy & Neurosciences, MS Center Amsterdam, Amsterdam Neuroscience, Amsterdam UMC, Vrije Universiteit Amsterdam, Amsterdam, Netherlands

³ Department of Medical, Health and Neuropsychology, Leiden University, Leiden, Netherlands

⁴ Department of Imaging Physics, Delft University of Technology, Delft, Netherlands

E-mail: d.karkalousos@amsterdamumc.nl

Keywords: MRI; Image Reconstruction; Machine Learning; Data Consistency; Compressed Sensing

Abstract

Interpretability and robustness are imperative for integrating Machine Learning methods for accelerated Magnetic Resonance Imaging (MRI) reconstruction in clinical applications. Doing so would allow fast high-quality imaging of anatomy and pathology. Data Consistency (DC) is crucial for generalization in multi-modal data and robustness in detecting pathology. This work proposes the Cascades of Independently Recurrent Inference Machines (CIRIM) to assess DC through unrolled optimization, implicitly by gradient descent and explicitly by a designed term. We perform extensive comparison of the CIRIM to other unrolled optimization methods, being the End-to-End Variational Network (E2EVN) and the RIM, and to the UNet and Compressed Sensing (CS). Evaluation is done in two stages. Firstly, learning on multiple trained MRI modalities is assessed, i.e., brain data with T₁-weighting and FLAIR contrast, and T₂-weighted knee data. Secondly, robustness is tested on reconstructing pathology through white matter lesions in 3D FLAIR MRI data of relapsing remitting Multiple Sclerosis (MS) patients. Results show that the CIRIM performs best when implicitly enforcing DC, while the E2EVN requires explicitly formulated DC. The CIRIM shows the highest lesion contrast resolution in reconstructing the clinical MS data. Performance improves by approximately 11% compared to CS, while the reconstruction time is twenty times reduced.

1. Introduction

Magnetic Resonance Imaging (MRI) non-invasively images the anatomy and pathology of the human body. The main advantages compared to Computer Tomography, for example, are the high soft-tissue contrast and the radiation-free nature of the technique. Data are acquired

in the frequency domain, known as k-space, where the measured signals need to adhere to the Nyquist-criterion to allow for inverse Fourier transforming them to the image domain without aliasing. Due to hardware limitations and physics constraints, sampling the full k-space leads to long scanning times. The acquisition may be accelerated by subsampling in k-space, but this makes the inverse problem of accelerated MRI reconstruction ill-posed; whereby it is unknown how we can restore a true image given sparsely sampled measurements.

Almost 25 years ago, Parallel-Imaging (PI) (Sodickson and Manning, 1997) was introduced to reduce acquisition times, overcoming hardware and software limitations by acquiring images from multiple receiver coil arrays with distinct coil sensitivity profiles, aiding in reconstructing undersampled data. In sensitivity encoding (SENSE), the multicoil data are transformed to the image domain through the inverse Fourier Transform, after which the individual coil images are combined with the coil sensitivity maps (Pruessmann et al., 1999). The combination of PI with Compressed Sensing (CS) (Donoho, 2006) has been successfully applied to the clinical setting, allowing for high acceleration factors by utilizing the constrained reconstruction through a sparsifying transform. While the acquisition times are reduced, the reconstruction times are increased because of the iterative reconstruction approach.

Machine Learning (ML) methods learn how to approximate the true image by training on data while reducing the reconstruction times, which is paramount not to obstruct the clinical workflow. The UNet (Ronneberger, Fischer and Brox, 2015) may be the most popular network in the field and the base for numerous other methods, as elaborated upon below. Its unique architecture, with the down- and up- sampling operators and the large number of features on the output, has made it a cornerstone in reconstruction today. Below, we provide a brief summary of how the field has been moving in recent past years.

In 2019, the fastMRI consortium organized a first reconstruction challenge on knee MRI data (Knoll et al., 2020). The winning method on reconstructing four and eight times accelerated multicoil data focused on enforcing Data Consistency (DC) (Pezzotti et al., 2020). The proposed Convolutional Neural Network (CNN) leverages the Iterative Shrinkage-Thresholding Algorithm (Beck and Teboulle, 2009) to learn strong priors by optimizing the sparsifying (wavelet) transform and thresholding through backpropagation, while enforcing DC with 2.5D convolutions. In a singlecoil track, the invertible Recurrent Inference Machines (RIM) (Putzky et al., 2019) scored on top by training a very deep Recurrent Neural Network (400 layers). The RIMs (Lønning et al., 2019) optimize through gradient descent and by explicitly modeling the forward model of accelerated MRI reconstruction, thus being physics-informed. Similarly, the Sigma-Net (Schlemper et al., 2019) explored several ways of enforcing DC and modeling coil sensitivity maps for robust reconstruction of multicoil data through unrolled optimization.

Robustness when reconstructing multicoil data with varying number of coils was the objective of the Multi-channel Magnetic Resonance Reconstruction (MC-MRRec) Challenge (Beauferris et al., 2020), hosted by the Calgary-Campinas group. The RIM scored highest on all tracks, while other submissions used UNet-based architectures, dual-domain networks (Souza et al., 2020), and large models trained through an increasing number of cascades (Souza et al., 2019). Methods such as the RIM, the Sigma-Net, the Model-Based Deep Learning network (Aggarwal, Mani and Jacob, 2019), and the Variational Network (VN)

(Hammernik et al., 2018) learn how to solve the inverse problem of accelerated MRI reconstruction through a Bayesian estimation. The strength of these approaches is the generalization on diverse datasets, including multiple image modalities and a varying number of coils and matrix sizes.

Generalization to a large diverse dataset was the objective at a challenge later in 2020 hosted by the fastMRI group, providing brain data containing pathologies. The End-to-End Variational Network (E2EVN) (Sriram, Zbontar, Murrell, Defazio, et al., 2020), the "Momentum Deep, Iterative, Hierarchical Network", and the RIM performed unrolled optimization to score among the top solutions. The XPDNet (Ramzi, Ciuciu and J.-L. Starck, 2020) was optimized by unrolling the Primal-Dual algorithm (Chambolle and Pock, 2011; Adler and Öktem, 2018) and using a Multi-Scale Wavelet CNN to denoise images. The Joint-ICNet combined a UNet and a KIKI-net (Eo et al., 2018), to operate both in k-space and the image domain. The network proposed by the AIRS medical team (Muckley et al., 2021) outperformed all other methods using a similar combination of a UNet and KIKI-net, while the main contribution can be seen to be the enforced interleaved DC on each layer.

Data consistency can be enforced through several ways when training ML networks, such as through gradient descent (Hammernik et al., 2018; Lønning et al., 2019; Schlemper et al., 2019; Sriram, Zbontar, Murrell, Defazio, et al., 2020), through an iterative energy minimization process (Duan et al., 2019), through Generative Adversarial Networks while limiting a pixel-wise or cyclic loss (Yang et al., 2018; Cole et al., 2020), and through CS-based methods (Quan, Nguyen-Duc and Jeong, 2018). Combining traditional iterative methods with neural networks, such as in the ADMM-Net (Yang et al., 2017), the GRAPPA-Net (Sriram, Zbontar, Murrell, Zitnick, et al., 2020), and the Total Variation Inspired Network (Zhang et al., 2020), can also help to enforce DC through sparsity, at the cost of increased reconstruction times. AUTOMAP assessed DC and further generalization by manifold approximation (Zhu et al., 2018). Complex-valued networks have also been proposed for enforcing DC while allowing more accurate phase reconstruction, which is necessary for tasks like fat-water separation and flow quantification (Wang et al., 2020; Cole et al., 2021).

While ML methods allow for fast acquisition and reconstruction, it is not ensured that they yield robustness in image reconstruction. The observed hallucinations and artifacts in reconstructed images, particularly when deviating from the training data, still need to be better understood (Johnson et al., 2021). Embedding DC in networks while balancing the degree of network complexity are crucial aspects to be considered in further designing machine learning schemes towards use in the clinical setting.

In this work, we propose a new scheme called Cascades of Independently Recurrent Inference Machines (CIRIM). The CIRIM comprises RIM blocks connected sequentially through cascades and the Independently Recurrent Neural Network (IndRNN) (Li et al., 2018) as recurrent unit. Interleaved DC is explicitly enforced to test the RIM's efficiency on implicitly evaluating the gradient of the prior and not the prior itself. For this purpose, we compare CIRIM's behavior to the End-to-End Variational Network (E2EVN) targeting unrolled optimization and testing enforced DC by gradient descent and by an explicitly formulated term. The performance of those methods is evaluated on trained multi-modal MRI datasets and further compared to the RIM built with the IndRNN, the baseline UNet, and

Compressed Sensing. The training datasets contain T1- and FLAIR- scans of brains and Proton Density FSE scans of knees. Finally, we set a clinical scenario and test performance on reconstructing out-of-training distribution data of Multiple Sclerosis patients containing lesions. We target fast reconstruction and thus assess inference time against model complexity.

2. Methods

In this section, first, the background on solving the inverse problem of accelerated MRI reconstruction through a Bayesian approach is set. In 2.2.1 and 2.2.2, unrolled optimization by gradient descent analyzes the End-to-End Variational Network (E2EVN) and the Recurrent Inference Machines (RIM). The Cascades of Independently Recurrent Inference Machines (CIRIM) is proposed, in 2.2.3, to assess Data Consistency (DC) implicitly and explicitly by a formulated DC term. In 2.2.4, the loss function is explained with respect to the network's architecture. In 2.3, the experiments are described, i.e., the datasets, the evaluation metrics, and the hyperparameters search to find best networks' architectures and interpret networks' behavior.

2.1. The inverse problem of accelerated MRI reconstruction

The objective when solving the inverse problem of accelerated MRI reconstruction (Figure 1) is to map the sparsely sampled k-space measurements to an unaliased image. Let the true image be denoted by $\mathbf{x} \in \mathbb{C}^n$ with $n = n_x \times n_y$, and let $\mathbf{y}_t \in \mathbb{C}^m$, $m \ll n$, be the set of the sparsely sampled data on k-space of the t -th coil for total c receiver coils. The forward model describes how the measured data are obtained from an underlying reference image, as formulated in the following equation:

$$\mathbf{y}_t = \mathbf{P} \mathcal{F} \mathbf{S}_t \mathbf{x} + \mathbf{n}_t, \quad t=1, \dots, c. \quad (1)$$

\mathbf{S}_t denotes the coil sensitivity maps, a diagonal matrix of the spatial sensitivity that scales every pixel of the reference image by a complex number. The Fourier transform \mathcal{F} projects the image onto k-space, where a sub-sampling mask \mathbf{P} selects a fraction of samples to reduce scan time. \mathbf{n}_t ($n_t \sim N(0, I\sigma^2) + iN(0, I\sigma^2)$, $i^2=-1$) denotes further unspecified accumulated measurement noise added by the scanner.

The inverse transformation of restoring the true image from the set of the sparsely sampled measurements can be found through the Maximum A Posteriori (MAP) estimator, given by

$$\mathbf{x}_{MAP} = \text{argmax}_{\mathbf{x}} \{ \log p(\mathbf{y}|\mathbf{x}) + \log p(\mathbf{x}) \}, \quad (2)$$

which is the maximization of the sum of the log-likelihood and the log-prior distribution of \mathbf{y} and \mathbf{x} , respectively. The log-likelihood represents the forward process of corrupting k-space measurements, while the log-prior distribution restricts the solution space by representing an MR-image's likely appearance.

Conventionally, (2) is reformulated as the following optimization problem,

$$x_{MAP} = \operatorname{argmin}_x \left\{ \sum_{i=1}^c d(y_i, PFS_i x) + \lambda R(x) \right\}, \quad (3)$$

where \mathbf{d} ensures data consistency between the reconstruction and the measurements, reflecting the error distribution given by the log-likelihood distribution in (2). \mathbf{R} is a regularizer with factor λ , which further limits the solution space for an ill-posed problem by representing prior knowledge over x .

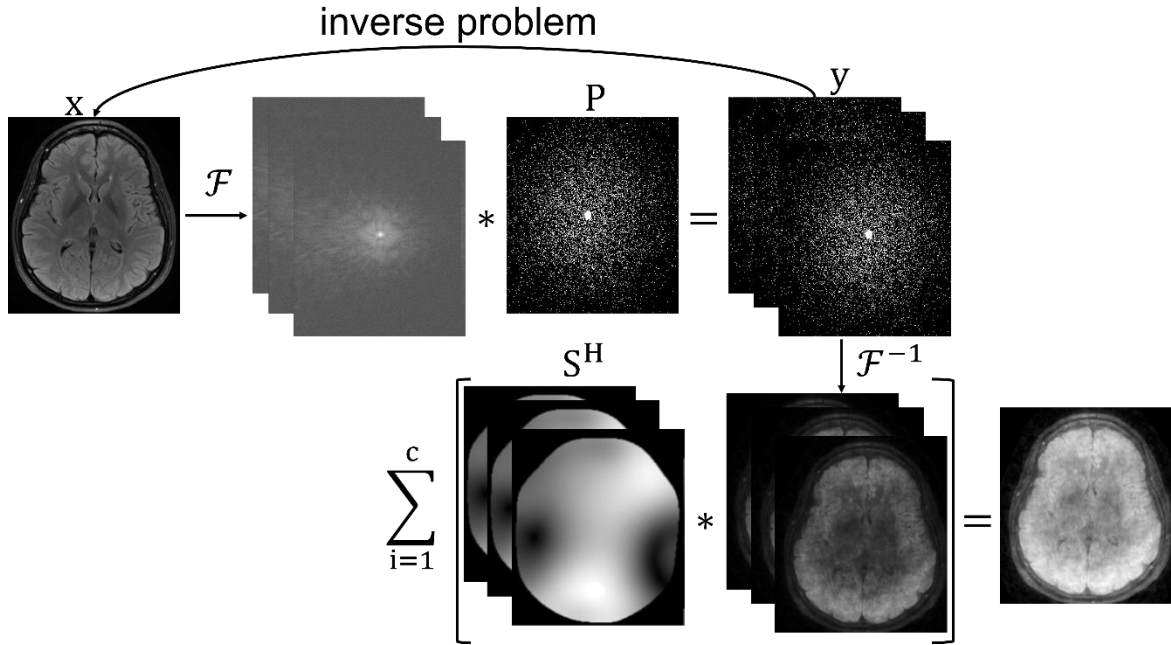


Figure 1: The goal in accelerated MRI reconstruction is to solve the inverse problem of recovering an unaliased image (x) from the set of sparsely sampled measurements (y). A forward model starts from the true image representation x (top-first), measured over multiple receiver coils S (bottom-first). It is Fourier transformed onto k -space (top-second) and sub-sampled using a mask P (top-third) to obtain sparsely sampled measurements y (top-fourth). Through the inverse Fourier transform (bottom-second) and after combining with coil sensitivity maps (bottom-first), an aliased image is obtained (bottom-third).

2.2. Unrolled optimization by gradient descent

Gradient descent is a default method for minimizing differentiable functions. Unrolled optimization to the regularized problem (3) is performed over T iterations or time-steps, given by

$$x_{\tau+1} = x_{\tau} - \gamma_{\tau} \nabla (\log p(y | x) + \log p(x)), \quad (4)$$

for time-step τ , $0 \leq \tau < T$, where γ is the learning rate. Assuming Gaussian distributed data and ignoring the regularization term here, the (negative) log-likelihood is given by:

$$\log p(y | x) = \frac{1}{\sigma^2} \sum_{i=1}^c \|PFS_i x - y_i\|_2^2 \quad (5)$$

$$= \frac{1}{\sigma^2} \| \mathbf{A}(\mathbf{x}) - \mathbf{y} \|_2^2, \quad (6)$$

where \mathbf{A} denotes the linear forward operator of modeling the corruption process \mathbf{PFS} for multicoil data. The optimization now needs to accommodate for the complex-valued nature of the data.

2.2.1 Variational Network

The Variational Network (VN) (Hammerl et al., 2018) introduces a mapping to real-valued numbers, going from mapping $C^n \mapsto C^m$ to mapping $R^{2n} \mapsto R^{2m}$. Then, by least-squares minimization (6), \mathbf{x} can be computed. As originally proposed in (Chen, Yu and Pock, 2015) and adapted by the VN, the idea is to perform gradient descent through the iterative Landweber algorithm, given by

$$\mathbf{x}_{\tau+1} = \mathbf{x}_{\tau} - \gamma_{\tau} (\mathbf{A}^* (\mathbf{A}(\mathbf{x}_{\tau}) - \mathbf{y})), \quad (7)$$

where \mathbf{A}^* is the Hermitian adjoint operator of \mathbf{A} . (3) can now be written as

$$\mathbf{x}_{\tau+1} = \mathbf{x}_{\tau} - \gamma_{\tau} (\mathbf{A}^* (\mathbf{A}(\mathbf{x}_{\tau}) - \mathbf{y}) + \lambda \mathbf{R}(\mathbf{x})). \quad (8)$$

Now, the regularizer \mathbf{R} needs to be defined for formulating (8) as a trainable gradient scheme with time-varying parameters. The vanilla VN adapts a generalization of Total-Variation, the Field of Experts model. In (Sriram, Zbontar, Murrell, Defazio, et al., 2020), the End-to-End Variational Network (E2EVN) uses a UNet as regularizer \mathbf{R} , where its parameters and γ are learned from the data.

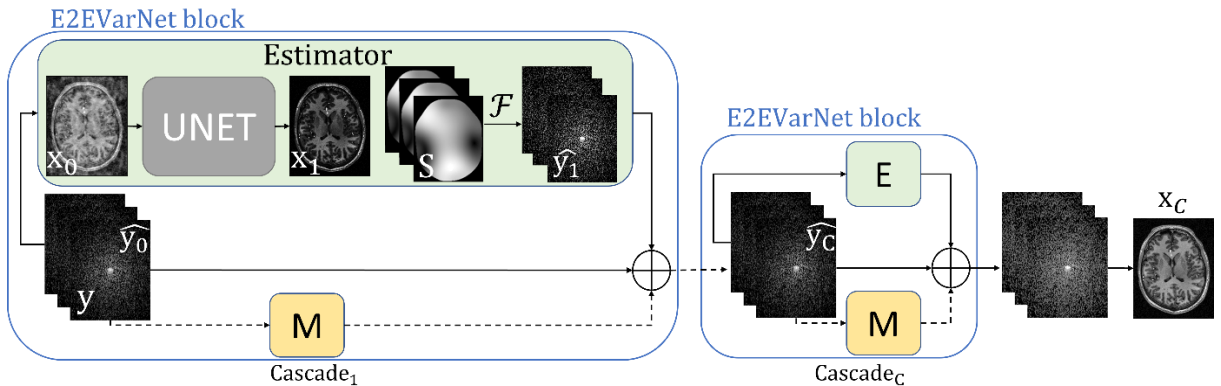


Figure 2: The End-to-End Variational Network. The input to the model is the set of sparsely-sampled measurements \mathbf{y} (bottom-left). The input to the Estimator (E) is the linear reconstruction, \mathbf{x}_0 (top-left), which is given as input to the regularizer (UNET). The output is then multiplied by the coil sensitivities maps and Fourier transformed back to k-space. Data Consistency (DC) is enforced by the operator \mathbf{M} (15). Enforcing DC can be skipped by omitting \mathbf{M} . For the first cascade, $\widehat{\mathbf{y}}_0$ is equal to the reference k-space \mathbf{y} . Finally, the predicted k-space is inverse transformed to image space and combined with coil sensitivities maps to produce the model's estimate \mathbf{x}_C .

The complex- to complex- valued mapping is performed in image space by concatenating the real-valued data along the coil dimension and transforming them into complex-valued after the UNet approximation. The gradient of the regularization, though, is applied in image space since the output of the UNet is the magnitude image (Figure 2).

2.2.2 The Recurrent Inference Machines (RIM)

The RIMs target optimization through complex-valued parametrization, which requires derivation with respect to a complex variable. This can be achieved using the Wirtinger- or $\mathbb{C}\mathbb{R}$ - calculus (Amin et al., 2011; Sarroff, Shepardson and Casey, 2015; Zhang and Mandic, 2016). Gradient descent can be performed using a real-valued cost function of complex variables using the Wirtinger derivative, even though the function does not have a complex derivative.

As a result, and as proposed in (Lønning et al., 2019), the gradient of the log-likelihood in (5) at time-step τ , can be formulated as follows

$$\nabla_{y|x_\tau} := \frac{1}{\sigma^2} \sum_{i=1}^c S_i^H \mathcal{F}^{-1} P^T (P \mathcal{F} S_i x_\tau y_i). \quad (9)$$

In (Andrychowicz et al., 2016), a novel method was proposed for non-convex optimization problems. Here, update rules are learned by the optimizer \mathbf{g} , specified by its own set of parameters φ , resulting in updates of the form

$$x_{\tau+1} = x_\tau + g_\tau(\nabla f(x_\tau), \varphi). \quad (10)$$

The advantage is the explicit modeling of the update rule g using a Recurrent Neural Network (RNN), which maintains its state and dynamically updates its iterations.

The Recurrent Inference Machines (RIM) (Putzky and Welling, 2017) originally proposed as a generalization to the previous approach for solving inverse problems. Except for the gradient information, the model is aware of the absolute position of the estimation in variable space (10). Formulating (2) accordingly results in

$$x_{\tau+1} = x_\tau + g_\varphi(\nabla_{y|x_\tau}, x_\tau). \quad (11)$$

The update equation can be restored then with

$$g_\varphi(\nabla_{y|x}, x_\tau) = \gamma_\tau(\nabla_{y|x}, \nabla_x). \quad (12)$$

(12) shows that the prior $p_\varphi(x)$ is never explicitly evaluated, but instead its gradient when performing updates. The step size γ is learned implicitly in combination with the prior. Generalizing to (11), the RIM adheres to the RNN framework by adding a latent (hidden) state s_τ .

Finally, by inserting (9) into (11), the update equations of the RIM are obtained, given by

$$s_0 = 0, \quad x_0 = \sum_{t=1}^c S_t^H \mathcal{F}^{-1} P^T y_t, \quad (13)$$

$$s_{\tau+1} = h_{\varphi}^*(\nabla_{y|x_{\tau}}, x_{\tau}, s_{\tau}), \quad x_{\tau+1} = x_{\tau} + h_{\varphi}(\nabla_{y|x_{\tau}}, x_{\tau}, s_{\tau+1}).$$

h_{φ} consists of a sequence of alternating convolutional and recurrent layers. Through its recurrent nature and the recurrent unit, a notion of memory is maintained, discarding information deemed not helpful and retaining information that is considered beneficial.

h_{φ}^* is the updated model for state variable s . The unrolled scheme for producing updates is presented in Figure 3.

In previous work (Putzky and Welling, 2017; Lønning et al., 2019), the chosen method for the recurrent units was the Gated Recurrent Unit (GRU) (Cho et al., 2014). Here, we replace the GRU with the Independently Recurrent Neural Network (IndRNN) (Li et al., 2018) to reduce the number of model parameters while maintaining sufficient complexity for accurate reconstruction. Implementation notation for the units can be found in the Appendix.

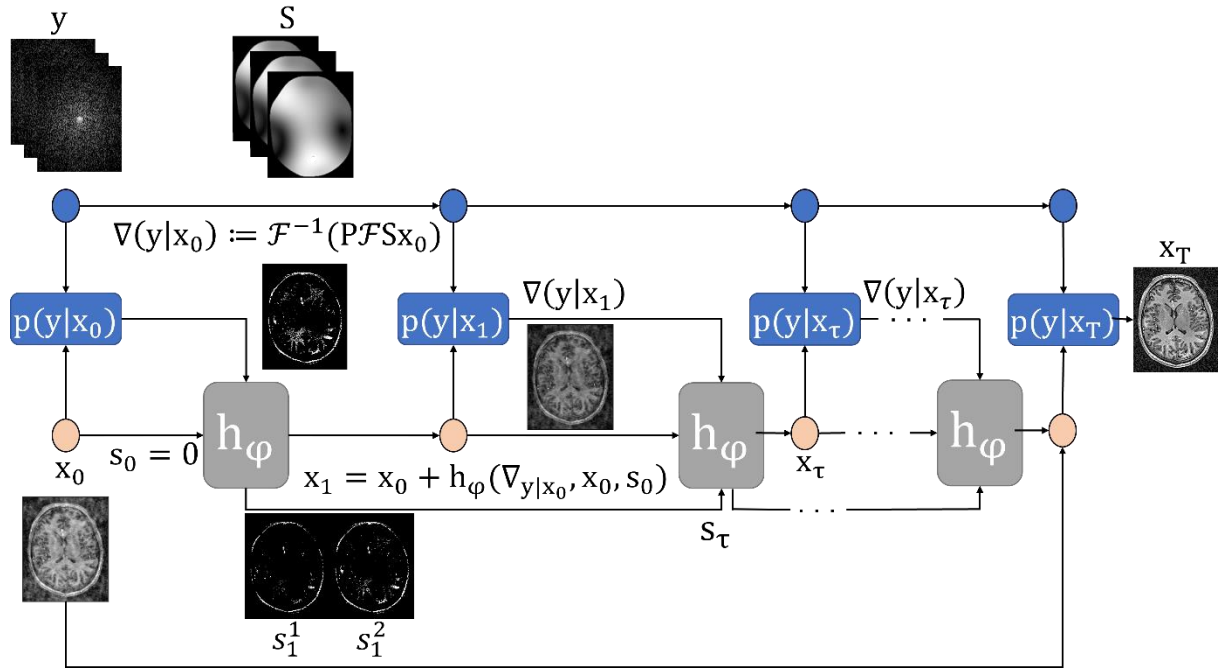


Figure 3: The Recurrent Inference Machines unrolled over time-steps (T). The inputs to the model are the set of sparsely sampled measurements y (top-left) and the initial estimation x_0 (bottom-left) for the estimation of the log-likelihood gradient (llg). The llg is passed through the network h_{φ} to produce updates, where the hidden states are initialized to $s_0 = 0$ and $s_{\tau+1} = 0$ for updating the model. At each time step τ the network updates itself for a total number of T to produce the estimation x_T (right).

2.2.3 Data Consistency

We now propose the Cascades of Independently Recurrent Inference Machines (CIRIM), consisting of sequentially connected RIM blocks (Figure 4). If the number of cascades equals

to one, then the CIRIM reverts to the baseline RIM using the IndRNN as recurrent unit (IRIM). For all models, the initial estimation is formulated in the same way, given by (13) and x_0 . For cascade C, x_C is given as input to the regularizer R. For the E2EVN, the UNet acts as R, while for the RIM the model itself acts as R.

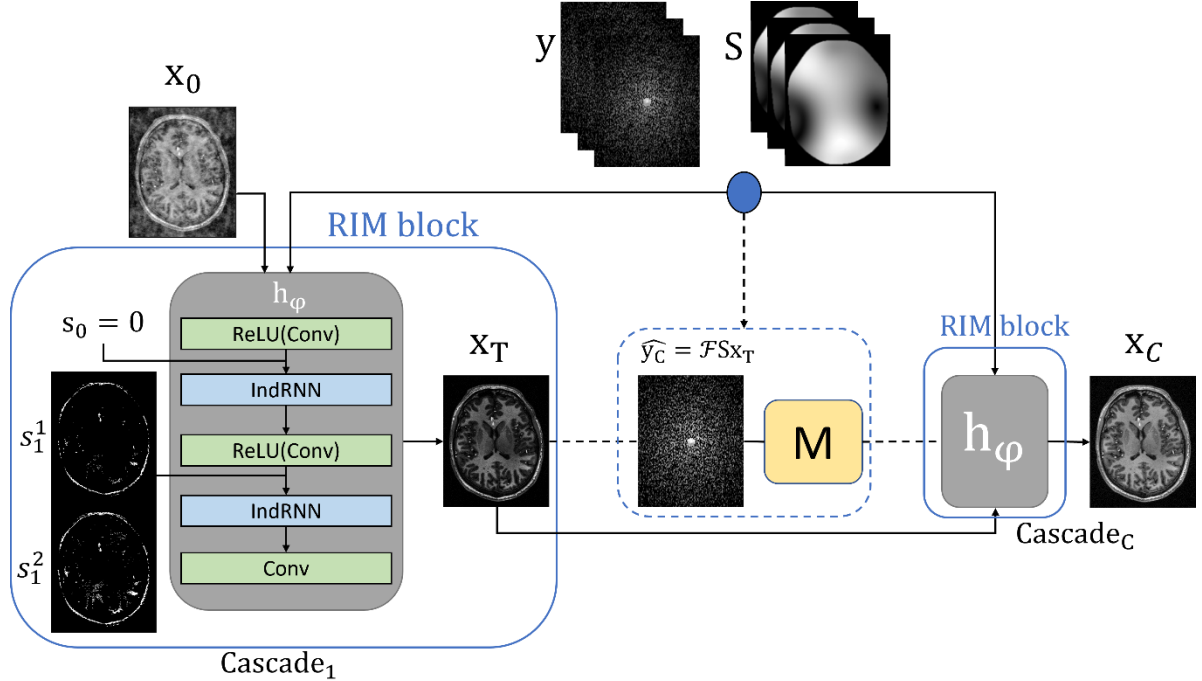


Figure 4: Cascades of Independently Recurrent Inference Machines (CIRIM). The output of the RIM (x_T) (*Cascade₁*, middle-right) is passed as estimation to a subsequent sequentially connected cascade to produce a final estimation over a total number of cascades C. Interleaved Data Consistency can be enforced by the operator M (14) after each cascade. In that case, the estimation of a RIM block is Fourier transformed to k-space and subtracted from the reference k-space y and the data consistency term (15) (not shown).

A soft DC term is explicitly formulated to balance the subsampled input measurements, y, and the predicted signals, \widehat{y}_{c-1} , given by

$$M = \lambda((y - \widehat{y}_{c-1}) \rightarrow P), \quad (14)$$

where, from (3), P is the subsampling mask and λ is a factor weighting the DC term.

Now, (8) needs to be satisfied to refine the prediction in k-space and explicitly enforce the DC-term in (14). This step is formulated as

$$\widehat{y}_c = y_{c-1} - M + A(R(x_c)), \quad (15)$$

where $A(R(x_c))$ denotes the FFT of the output combined with the coil sensitivity maps, y_{c-1} is the k-space prediction of the previous cascades and \widehat{y}_c the current prediction. For the E2EVN, (16) is satisfied in the Estimator block (Figure 2). For the CIRIM, it is interleaved between the cascades and applied only the DC step is performed.

The final output of the models is the sum of the inverse Fourier transformed prediction to the image space and combined with the coil sensitivity maps. If the step in (15) is omitted, the final output is given by $R(x_c)$.

2.2.4 Loss function

For calculating the loss, we compare normalized magnitude images derived from the complex-valued estimations x_τ against the fully sampled reference x . As loss function, we choose the ℓ_1 -norm as a more efficient metric for generalizing when solving high-dimensional problems, such as image reconstruction (Aggarwal, Hinneburg and Keim, 2001).

The ℓ_1 -norm represents the sum of the absolute difference between the estimate x_τ and the reference image x , given by

$$\mathcal{L}^{\ell_1}(x_T) = |x_\tau - x|. \quad (16)$$

For the CIRIM and the IRIM, the loss is weighted depending on the number of time-steps. Therefore, it is formulated as

$$\mathcal{L}^{\ell_1}(x_T) = \frac{1}{pT} \sum_{\tau=1}^T w_\tau |x_\tau - x|, \quad (17)$$

where p is the total number of pixels of the image and w_τ is a weight vector of length T , prioritizing the loss at latter time-steps. The weights were calculated by setting $w_\tau = 10^{-\frac{T-\tau}{T-1}}$.

2.3. Experiments

2.3.1 Datasets

For our experiments, we obtained multiple datasets. Scanning parameters are given in Table 1. In summary: (A) for training, validation, and evaluation, fully sampled data were acquired and retrospectively undersampled; (B) for independent evaluation, we used prospectively undersampled data of Multiple Sclerosis patients to study the effect of small perturbations unseen during training, such as lesions.

For objective (A), three fully sampled raw complex-valued multi-coil datasets were obtained. The first dataset was acquired in-house. To this end, 12 healthy subjects were included, from whom written informed consent (under an institutionally approved protocol) was obtained beforehand. The ethics board of Amsterdam UMC declared that this study was exempt from IRB approval. All 12 subjects were scanned by performing 3D T_1 -weighted brain imaging on a 3.0T Philips Ingenia scanner (Philips Healthcare, Best, The Netherlands) in Amsterdam UMC. The data were visually checked to ascertain that they were not affected by motion artifacts. After, raw data were exported and stored for offline reconstruction experiments. The training set was composed of ten subjects (approximately three thousand slices) and the validation set of one subject (approximately three hundred slices).

The second dataset consisted of 451 FLAIR scans, publicly available through the fastMRI brains dataset (Muckley et al., 2020). The training set consisted of 344 scans (approximately five thousand slices) and the validation set of 107 scans (approximately five hundred slices). The number of coils varied from 2 to 24. The data were cropped in the image domain to 320 for the readout direction by the size of the phase encoding direction (varied from 213 to 320).

The third dataset was composed of 3D knee scans of 20 subjects, available on a public repository (Epperson et al., 2013). From these data, one subject was discarded due to observed motion artifacts. The training set consisted of 17 subjects (approximately twelve thousand slices) and the validation set of one subject (approximately seven hundred slices).

Table 1: Scan parameters of each dataset used for different experiments. Target anatomy, contrast, scan, and field strength are given, with resolution (res), Field-of-View (FOV), time in minutes (with acceleration factor), number of coils (ncoils) and other scan parameters.

scan	sequence	field strength	res (mm)	FOV (mm)	time (acc)	ncoils	parameters
Training, validation							
brain 3D	T ₁ MPRAGE	3T	1.0x1.0x1.0	256x256x240	10.8	32	FA 9°, TFE-factor 150, TI=900ms
knee 3D	T ₂ TSE	3T	0.5x0.5x0.6	160x160x154	15.3	8	FA 90°, TR=1550ms, TE=25ms
brain 2D	FLAIR	1.5T/3T	0.7x0.7	220x220	1	2-24	FA 150°, TR=9000ms, TE=78-126ms
Pathology study							
brain 3D	FLAIR	3T	1.0x1.0x1.1	224x224x190	7.5	32	TR=4800ms, TE=350ms, TI=16500ms

The training and validation datasets were generated by randomly dividing slices of all subjects. The coil sensitivities were estimated using an autocalibration procedure called ecalib from the BART toolbox (Uecker et al., 2015), which leverages the ESPIRiT algorithm (Uecker et al., 2014). For all datasets and each subject, the volumes were normalized to the maximum magnitude. The 3D datasets were Fourier transformed along the frequency encoding axis and used as separate slices along the two-phase encoding axes. Then all data were retrospectively undersampled in 2D as follows.

k-space points were sampled from a two-dimensional Gaussian distribution with a Full Width at Half Maximum (FWHM) of 0.7, relative to the k-space dimensions; thereby prioritizing the sampling of low frequencies whereas creating incoherent noise due to the randomness. In this way, we abide by the Compressed Sensing (CS) requirement of processing incoherently sampled data (Lustig, Donoho and Pauly, 2007). For autocalibration purposes, data points near the k-space center were fully sampled within an ellipse of which the half-axes were set to 2% of the fully sampled region. Acceleration factors of 4x, 6x, 8x, and 10x (Figure 1, top-third (P)) were used to randomly generate masks during training and validation by setting a seed number.

For every scan, the Signal-to-Noise Ratio (SNR) was calculated as follows. The signal level was obtained by taking the mean value after thresholding the magnitude image to discard the background. The noise level was computed as the median magnitude value within a square region in the periphery of k-space, which was assumed to be dominated by imaging noise. These two ratios were taken as SNR estimates, across which the mean and standard deviation per training modality were computed. Reported values for the training datasets were 26 ± 5 for the T₁-weighted brains dataset, 24 ± 5 for the FLAIR brains dataset, and 17 ± 5 for the T₂-weighted knees dataset.

Finally, the models' ability to reconstruct unseen pathology is tested, c.f. objective (B). For this purpose, 3D FLAIR data of relapsing remitting Multiple Sclerosis patients with known white matter lesions were obtained. Data were prospectively undersampled with a factor of 7.5x on a Variable-Density Poisson disk distribution and acquired on a 3.0T Philips Ingenia scanner (Philips Healthcare, Best, The Netherlands) in Amsterdam UMC, within the scope of a larger, ongoing study. The local ethics review board approved this study and patients provided informed consent prior to imaging. A fully-sampled reference scan was also acquired and used to estimate coil sensitivity maps using the caldir method of the BART toolbox.

2.3.2 Evaluation metrics

For quantitative evaluation of the fully-sampled measurements, we compare normalized magnitude images derived from the complex-valued estimations x_{τ} against the reference x . We, therefore, calculate the Structural Similarity Index Measure (SSIM) (Wang et al., 2004) and the Peak Signal-to-noise ratio (PSNR) across the images.

For evaluating robustness on the 3D FLAIR MS data, we calculate the Contrast Resolution (CR). Since those data are not fully-sampled in the center, the CR is an efficient metric to evaluate the signal level between the white matter and the lesions. The lesion segmentations were performed at the Vrije Universiteit Medical Center (VUMC), using a Convolutional Neural Network (CNN) created for the segmentation of lesions in MS patients (Strijbis et al., 2021). For the segmentation of the white matter, the Statistical Parametric Mapping (SPM) toolbox was used (Penny et al., 2007). The lesion masks were dilated by four voxels to compare the lesion signal only to the surrounding white matter area. The comparison, thereby, focused on the most critical regions when segmenting lesions. Those were the border regions of the overlapping dilated areas with the white matter mask, as the segmented white matter is not necessarily homogeneous.

The CR is defined as the difference between the lesion signal and the signal in the white matter surrounding it, divided by the summation of them, given by

$$CR = \frac{S_{\text{lesion}} - S_{\text{WM_surrounding_lesion}}}{S_{\text{lesion}} + S_{\text{WM_surrounding_lesion}}}. \quad (18)$$

2.3.3 Hyperparameters

The hyperparameters of the CIRIM models were selected as follows. The number of channels set to 64 for the recurrent and convolutional layers, and the number of time steps T to 8. The

kernel size of the first convolutional layer was set to 5×5 and to 3×3 for the second and third layers. The optimization of those hyperparameters is described elsewhere (Lønning et al., 2019). Next, we trained models on the T_1 - weighted brains dataset to realize the DC step on (15) and select the number of cascades. For this, we tested values between 2, 3, 4, 5, 6, and 8 cascades for building CIRIM models.

For the E2EVN models, we trained models on the T_1 - weighted brains dataset as well and tested several combinations. As a starting point, we used the best proposed configurations reported in previous work (Sriram, Zbontar, Murrell, Defazio, et al., 2020; Muckley et al., 2021). Those were 12 cascades, 4 pooling layers, 18 channels for the convolutional layers, and including the DC step on (15). Then for further optimization, we experimented with omitting the DC step, reducing cascades to 8, pooling layers to 2, and the number of channels for the convolutions to 10 and 14. The inputs to the UNet regularizer were padded for making square inputs, setting the padding size to 11, and the outputs were unpadded for restoring the original input size.

For the baseline UNet, the number of input and output channels was set to 2. The number of channels for the convolutional layers was set to 64, and we chose 2 pooling layers. Same as for the E2EVN the padding size was set to 11, while no dropout was applied. The selected hyperparameters for the UNet were motivated by the configuration in (Zbontar et al., 2018).

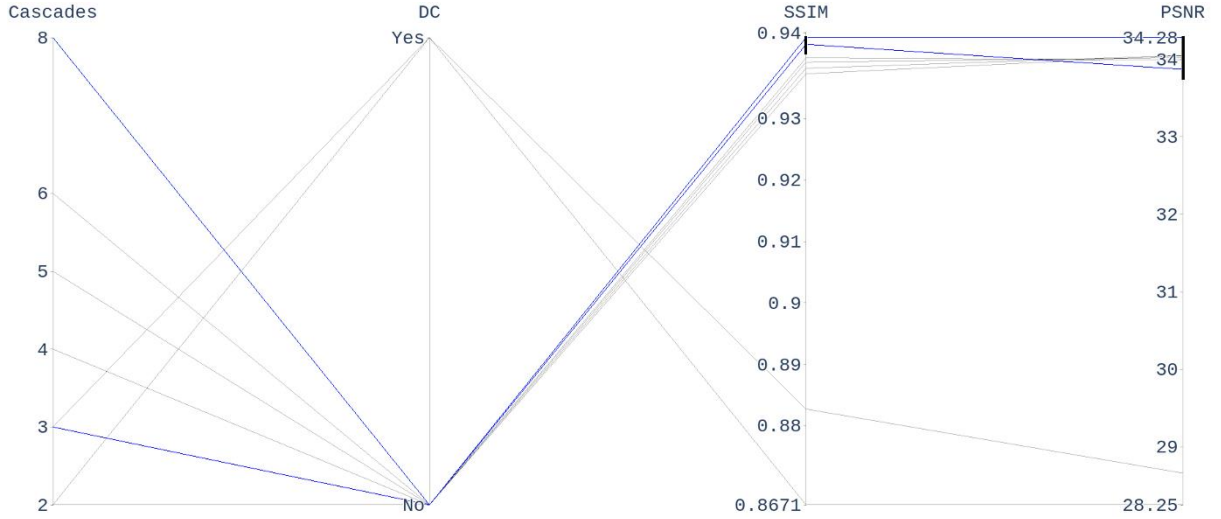
For all models, we applied the ADAM optimizer (Kingma and Ba, 2015), setting the learning rate to 1e-3. The data type was set to complex64 for complex-valued data and to float32 for real-valued data. Finally, the batch size was set to 1, allowing training on various input sizes. The code was implemented in the PyTorch 1.9 framework (Paszke et al., 2019) and can be found online at <https://github.com/wdika/mridc> (Karkalousos and Caan, 2021).

CS reconstructions were performed using the BART toolbox (Uecker et al., 2015). Here we used Parallel-Imaging Compressed Sensing (PICS) with a ℓ_1 -wavelet sparsity transform. The regularization parameter was set to $\alpha=0.005$, which was heuristically determined as a trade-off between aliasing noise and blurring. The maximum number of iterations was set to 60. For a fair comparison, we tested the reconstruction times of CS on the GPU (turning the -g flag on) and not on the CPU as conventionally.

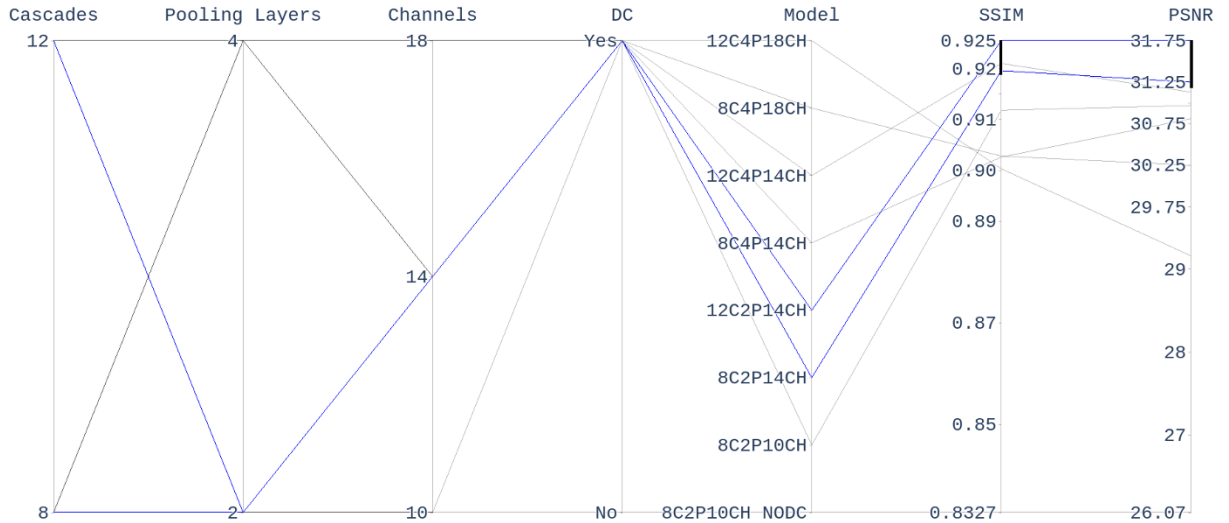
All experiments were performed on an Nvidia Tesla V100 with 32GB of memory.

Results

Figure 5 summarizes training models on the T_1 - weighted brains dataset for hyperparameters selection and evaluation of the Data Consistency (DC) term. For the CIRIM (Figure 5.a), including the DC term (DC – Yes) downgraded performance significantly. The best CIRIM models were those built with eight and three cascades. The best E2EVN models were trained with 8 and 12 Cascades, 2 Pooling layers, 14 CHannels, and DC enabled (Model 8C2P14CH and Model 12C2P14CH). For the E2EVN (Figure 5.b), opposite to the CIRIM, omitting the DC term (Model 8C2P10CH NODC) reduced performance remarkably.



(a) CIRIM



(b) E2EVN

Figure 5: Overview of trained CIRIMs (a) and E2EVNs (b) on the T_1 - weighted brains dataset with resulting SSIM and PSNR scores. The parallel coordinates correspond to all tested values for finding the best hyperparameters. For (a) CIRIM, the number of cascades varies between 2 and 8. DC (15) is either included or excluded (DC –Yes/No). For (b) E2EVN, the combination of Cascades C, Pooling Layers P, Channels CH, and DC (by default DC-Yes, otherwise DC-No) concludes to the Model. The best models’ parallel coordinates are highlighted, while the bold vertical line on SSIM and PSNR highlights the best scoring range.

Table 2 summarizes performance on the trained datasets. Here, the best CIRIM and E2EVN models are compared to the IRIM (a baseline RIM with the IndRNN as recurrent unit), the UNET, and PICS. The CIRIM 8C yielded the highest SSIM and PSNR on the T_1 -weighted brains dataset and the highest PSNR on the FLAIR brains dataset. The CIRIM 3C scored the highest SSIM on the FLAIR dataset. For the T_2 - knees dataset, the E2EVN 12C scored the highest SSIM and the E2EVN 8C scored the highest PSNR, albeit with a marginal increase over the CIRIM. The UNET and PICS scored significantly worse than all other methods.

Table 2: SSIM & PSNR scores of all methods evaluated for ten times acceleration, on the validation set of each trained dataset. First column reports the method's name (with a number of cascades C). The second column reports the total number of trainable parameters for each model. Best performing models are highlighted in bold.

Method	Params	T ₁ -weighted Brain		FLAIR Brain		T ₂ -weighted Knee	
		SSIM ↑	PSNR ↑	SSIM ↑	PSNR ↑	SSIM ↑	PSNR ↑
CIRIM 3C	160k	0.941±0.037	33.9±2.6	0.901±0.089	32.0±4.9	0.846±0.050	30.7±1.8
CIRIM 8C	420k	0.943±0.036	34.3±2.9	0.899±0.085	32.1±4.8	0.853±0.045	31.9±2.4
E2EVN 8C	720k	0.920±0.042	31.3±3.2	0.814±0.106	24.8±4.3	0.852±0.044	32.0±2.3
E2EVN 12C	1.1M	0.926±0.043	31.8±3.0	0.770±0.122	24.3±4.2	0.855±0.046	31.8±2.1
IRIM	53k	0.940±0.036	34.1±2.6	0.892±0.089	31.3±5.0	0.850±0.045	31.7±1.9
PICS		0.874±0.050	31.9±2.9	0.862±0.154	31.7±7.0	0.676±0.032	29.5±3.5
UNET	1.8M	0.870±0.066	28.7±2.9	0.519±0.152	23.4±5.7	0.813±0.054	28.7±2.1

The abovementioned performance metrics are all presented for 10x accelerated data. Evaluations on the other trained factors (4x, 6x, and 8x) were analogous (results not shown). Example reconstructions of the T₁-weighted brains dataset, the FLAIR brains dataset, and the T₂- knees dataset can be found in the Supplementary material.

Next, as summarized in Table 3, performance is evaluated by measuring the contrast resolution on reconstructed lesions from the out-of-training-distribution 3D FLAIR brains dataset of MS patients. The CIRIMs and the IRIM trained on the brain datasets performed equivalently to PICS. Compared to PICS, the CIRIM with eight cascades (8C) trained on the FLAIR dataset improved performance by approximately 11%. The UNET was excluded due to inefficient reconstructions. The E2EVN models reported low CR, inadequate to realize improvement compared to the linear reconstruction. Also, training on knees appears to be inefficient for reconstructing brain lesions.

Table 3: Contrast Resolution (CS, higher is better) of MS lesions from the 3D FLAIR brains dataset. The first column reports methods (with cascades C). The second, third, and fourth columns report CR-scores with standard deviation for each model trained on the T₁-weighted Brains dataset, the FLAIR Brains dataset, and the T₂-weighted Knees dataset, respectively. The highest CR-score is highlighted in bold.

Method	CR of models trained on T ₁ - Brains data	CR of models trained on FLAIR Brains data	CR of models trained on T ₂ - Knees data
CIRIM 3C	0.170±0.025	0.162±0.025	0.071±0.025
CIRIM 8C	0.172±0.024	0.181±0.031	0.086±0.031
E2EVN 8C	0.074±0.024	0.072±0.024	0.072±0.022
E2EVN 12C	0.075±0.023	0.074±0.023	0.072±0.023
IRIM	0.175±0.024	0.163±0.024	0.068±0.022
PICS		0.178±0.025	

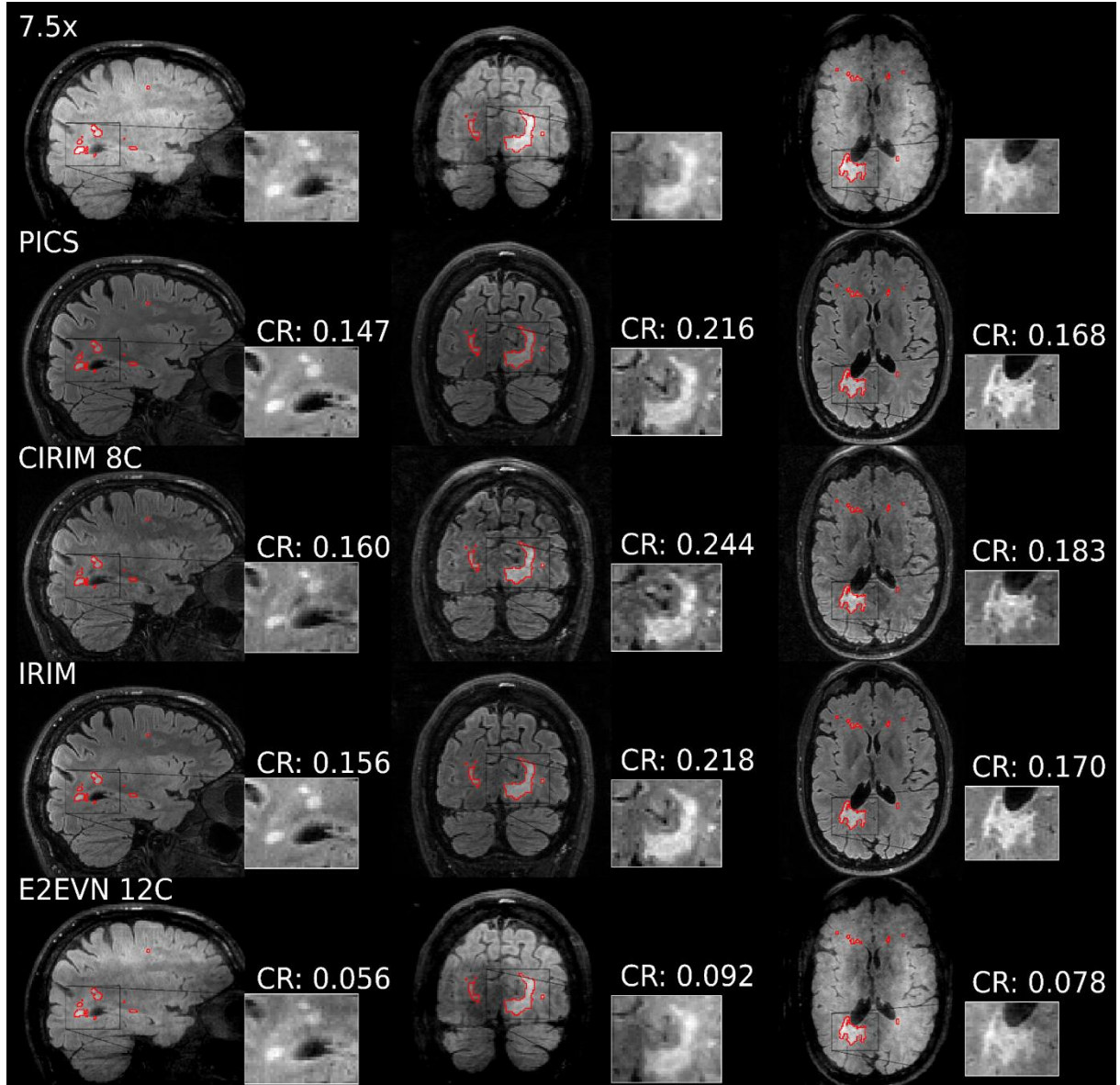


Figure 6: Reconstructions of a representative sagittal, coronal, and axial slice of accelerated 3D FLAIR scans of different MS patients in three columns. Segmented MS lesions are depicted with red colored contours. Shown is the aliased linear reconstruction of 7.5x accelerated data (first row), PICS (second row), and trained model reconstructions: the CIRIM 8C trained on the fastMRI FLAIR data (third row), the IRIM trained on T_1 -weighted brain data (fourth row) and the E2EVN with 12 cascades trained on T_1 -brain data (fifth row). The inset on the right bottom of each reconstruction focuses on a lesion region with high spatial detail. The Contrast Resolution (CR) is shown for all reconstructions (above each inset box).

Figure 6 shows example reconstructions of a sagittal slice, a coronal slice, and an axial slice of MS patients reconstructed using PICS, the CIRIM 8C trained on the FLAIR brain dataset, and the IRIM and the E2EVN 12C trained on the T_1 -weighted brain dataset. MS lesions appeared to be more blurred when reconstructed with PICS and the IRIM. The CIRIM 8C (third row) preserved a higher level of spatial detail, with an overall enhanced sharpness. For an individual slice, CR was improved from 8% (sagittal and axial slices) to 11% (sagittal slice) compared to Compressed Sensing. The E2EVN 12C did not show any significant improvement compared to the linear reconstruction (fifth row).

Finally, in Figure 7, the inference times of all methods are presented. The input was one volume from the trained fastMRI FLAIR brains dataset, consisting of fifteen slices and cropped to a matrix size of 320×320 . PICS was the slowest method, needed approximately 90 seconds to reconstruct the volume. The IRIM, the CIRIM 3C, the UNET, and the E2EVNs reported times from 200 ms to a second. Increasing the number of cascades for the CIRIM 8C linearly increased the inference time to approximately 5 seconds.

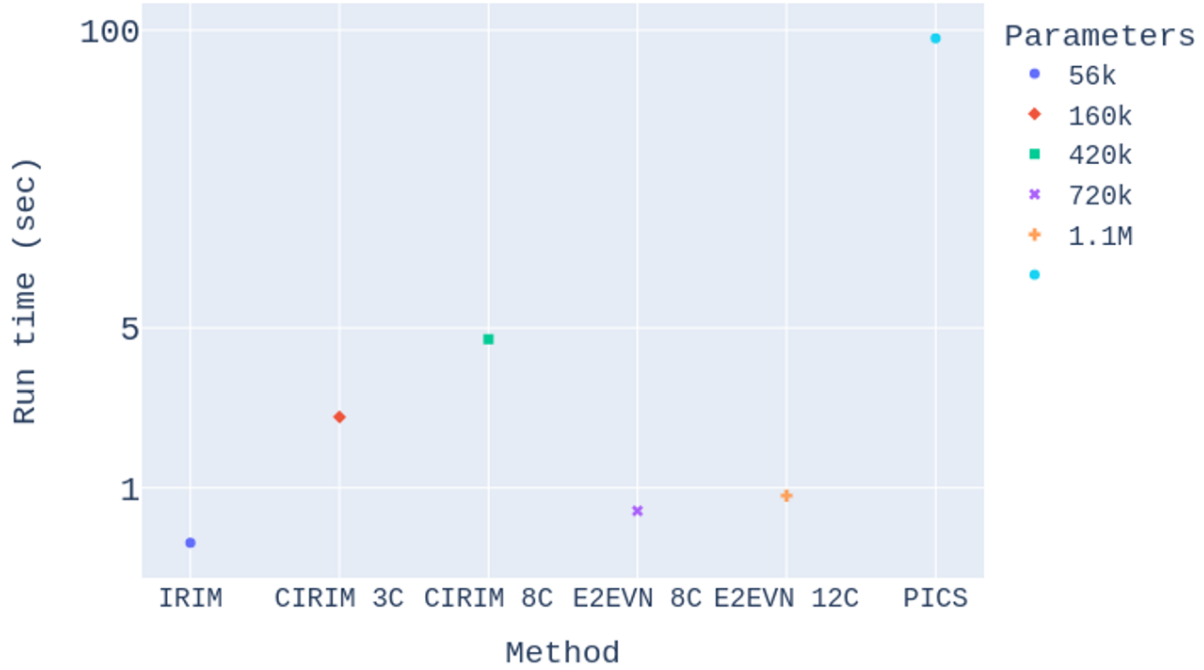


Figure 7: Inference times of reconstructing one volume from the FLAIR brains dataset. The x-axis represents model names with a number of cascades C. The total number of model parameters is reported on the right-hand side. The y-axis shows the run time in seconds.

3. Discussion

In this paper, we assessed Data Consistency (DC) through unrolled optimization by gradient descent and evaluated robustness on fast accurate reconstruction of out-of-training-distribution sparsely sampled MRI data containing unseen pathologies. To this end, we proposed the Cascades of Independently Recurrent Inference Machines (CIRIM) and compared to the End-to-End Variational Network (E2EVN), the Recurrent Inference Machines with the Independently Recurrent Neural Network (IndRNN) as recurrent unit (IRIM), the UNet and Compressed Sensing (CS). Implicitly, we also demonstrated generalization on deviating matrix sizes and a varying number of coils.

We experimented with reconstructing brain and knee data containing different contrasts. Results showed that the CIRIM and the lenient IRIM, trained on FLAIR and T_1 -weighted brain data, respectively, could accurately reconstruct Multiple Sclerosis lesions unseen during training. The proposed CIRIM scored the highest on measured Contrast Resolution with promising generalization capabilities, preserving spatial detail on reconstructing MS lesions with enhanced sharpness in contrast to a more blurred result by PICS. The E2EVN did not show any significant improvement to that end. The main reason for such behavior can be that

learning k-space corrections might be disadvantageous on data without a full sample center. The models trained on knees were inadequate in reconstructing MS lesions, indicating training anatomy preference rather than generalization.

The size of the training dataset appeared to be important regarding performance depending on models' size. The E2EVN with eight cascades was approximately two times larger than the CIRIM with the same number of cascades, while the E2EVN with twelve cascades was approximately three times larger. This reflected to some extent on the SSIM and PSNR scores on the trained datasets. The E2EVN models performed highest on the largest trained dataset, the T_2 -weighted knee dataset, which contained approximately twelve thousand slices. The CIRIM scored highest on the brains datasets, of T_1 -weighting and FLAIR contrast, which consisted of approximately three and five thousand slices, respectively. PICS scored overall lower than the Machine Learning (ML) methods, illustrating that learning a prior with an efficient model is advantageous. The UNet only performed better than PICS on the knees dataset. Furthermore, the overall SSIM and PSNR scores were higher and close on the brains dataset and reduced on the knees dataset. This could be to the fact of low SNR on the knee data (17 ± 5) compared to the higher SNR on the T_1 -weighted (26 ± 5) and the FLAIR (24 ± 5) brain datasets.

Importantly, our results show that the RIM-based models can reconstruct images unseen during training. The RIM explicitly formulates the prior information of an MR image and acts as optimizer itself. Unrolled optimization is performed by gradient descent by optimizing by gradient descent through time-steps (Putzky and Welling, 2017), thus enforcing DC implicitly. The CIRIM further evaluates the RIM estimation through the cascades without sharing parameters, as in previous work (Schlemper et al., 2018; Huang et al., 2019; Aghabiglou and Eksioglu, 2021). By applying the cascades, we can train a larger RNN and capture long-range dependencies without gradients vanishing or exploding. The E2EVN also performs unrolled optimization through gradient descent, but on each iteration, k-space corrections are performed with an explicitly formulated DC term and through a number of cascading layers. The difference is that the optimization is not learned, as for the RIM, but targeted. For the CIRIM, including the DC term after each cascade downgraded performance.

Reconstruction times were also realized as a crucial factor when applying any ML method to the clinical workflow. The time of reconstructing one volume from the FLAIR brains dataset with a conventional CS algorithm was approximately ninety seconds. The IRIM and the E2EVNs needed approximately half and one second, respectively. The CIRIM with eight cascades needed about five seconds. Recent work has pointed out the importance of benchmarking and quantifying the performance of such deep networks regarding the GPU memory required for training, the inference times, the applications, and the optimization (Wang et al., no date; Ramzi, Ciuciu and J. L. Starck, 2020; Hammernik et al., 2021).

Limitations of our work include the evaluation of learning coil sensitivity maps during training, matching exact models' sizes for all variations, and tuning the explicitly formulated DC term. Notably, exhaustive evaluations of the RIM and the E2EVN have been presented in previous work (Hammernik et al., 2018; Lønning et al., 2019; Putzky et al., 2019; Beauferris et al., 2020; Sriram, Zbontar, Murrell, Defazio, et al., 2020; Johnson et al., 2021; Muckley et al., 2021).

4. Conclusion

Interpretability of Machine Learning methods is crucial when applying them to the clinical setting, where a detailed explanation of the model's behavior is necessary to improve decision-making. Our work assessed robustness on accelerated MRI reconstruction using unrolled networks and explored enforcing Data Consistency implicitly by gradient descent and explicitly with a formulated term. We proposed the Cascades of Independently Recurrent Inference Machines (CIRIM) to test if unrolled optimization is targeted or enforced. Furthermore, we realized models' behavior on sharing parameters over time (-steps) with an optimizer, such as the Recurrent Inference Machines, and not sharing parameters through the cascades with an optimized network; being the End-to-End Variational Network (E2EVN). The E2EVN performed best when DC was explicitly enforced and optimized on the training distributions performance, but it was inadequate on reconstructing out-of-distribution data without a fully sampled center. The CIRIM performed best when DC was implicitly enforced by gradient descent. The proposed network optimized on training datasets and showed robust performance on reconstructing accelerated FLAIR data containing MS lesions, achieving a higher spatial detail and enhanced sharpness. To that extent, the impression is that evaluating the forward process of accelerated MRI reconstruction, frequently through time, is of great importance for generalization in other settings. The implemented cascades and the application of the RIM to a larger network allowed backpropagation on a smaller number of time-steps but on higher frequency for each iteration. Finally, all evaluated methods improved reconstruction speed more than twenty times compared to the used in practice CS, thus highlighting the substantial advantage of ML on reducing time in the clinical workflow.

Acknowledgments

This publication is based on the STAIRS project under the TKI-PPP program. The collaboration project is co-funded by the PPP Allowance made available by Health~Holland, Top Sector Life Sciences & Health, to stimulate public-private partnerships.

M.W.A. Caan is shareholder of Nico.Lab International Ltd.

References

Adler, J. and Öktem, O. (2018) "Learned Primal-Dual Reconstruction," *IEEE Transactions on Medical Imaging*, 37(6), pp. 1322–1332. doi:10.1109/TMI.2018.2799231.

Aggarwal, C.C., Hinneburg, A. and Keim, D.A. (2001) "On the surprising behavior of distance metrics in high dimensional space," *Lecture Notes in Computer Science* (including subseries *Lecture Notes in Artificial Intelligence* and *Lecture Notes in Bioinformatics*), 1973, pp. 420–434. doi:10.1007/3-540-44503-x_27.

Aggarwal, H.K., Mani, M.P. and Jacob, M. (2019) "MoDL: Model-Based Deep Learning Architecture for Inverse Problems," *IEEE Transactions on Medical Imaging*, 38(2), pp. 394–405. doi:10.1109/TMI.2018.2865356.

Aghabiglou, A. and Eksioglu, E.M. (2021) “Projection-Based cascaded U-Net model for MR image reconstruction,” Computer Methods and Programs in Biomedicine, 207, p. 106151. doi:10.1016/j.cmpb.2021.106151.

Amin, M.F. et al. (2011) “Wirtinger calculus based gradient descent and Levenberg-Marquardt learning algorithms in complex-valued neural networks,” Lecture Notes in Computer Science (including subseries Lecture Notes in Artificial Intelligence and Lecture Notes in Bioinformatics), 7062 LNCS(PART 1), pp. 550–559. doi:10.1007/978-3-642-24955-6_66.

Andrychowicz, M. et al. (2016) “Learning to learn by gradient descent by gradient descent,” Advances in Neural Information Processing Systems, (Nips), pp. 3988–3996.

Beauferris, Y. et al. (2020) “Multi-channel MR Reconstruction (MC-MRRec) Challenge -- Comparing Accelerated MR Reconstruction Models and Assessing Their Genereralizability to Datasets Collected with Different Coils,” arXiv, pp. 1–31. Available at: <http://arxiv.org/abs/2011.07952>.

Beck, A. and Teboulle, M. (2009) “A Fast Iterative Shrinkage-Thresholding Algorithm for Linear Inverse Problems *,” Society for Industrial and Applied Mathematics, 2(1), pp. 183–202. doi:10.1137/080716542.

Chambolle, A. and Pock, T. (2011) “A first-order primal-dual algorithm for convex problems with applications to imaging,” Journal of Mathematical Imaging and Vision, 40(1), pp. 120–145. doi:10.1007/s10851-010-0251-1.

Chen, Y., Yu, W. and Pock, T. (2015) “On learning optimized reaction diffusion processes for effective image restoration.”

Cho, K. et al. (2014) “Learning phrase representations using RNN encoder-decoder for statistical machine translation,” EMNLP 2014 - 2014 Conference on Empirical Methods in Natural Language Processing, Proceedings of the Conference, pp. 1724–1734. doi:10.3115/v1/d14-1179.

Cole, E. et al. (2021) “Analysis of deep complex-valued convolutional neural networks for MRI reconstruction and phase-focused applications,” Magnetic Resonance in Medicine, 86(2), pp. 1093–1109. doi:10.1002/mrm.28733.

Cole, E.K. et al. (2020) Unsupervised MRI Reconstruction with Generative Adversarial Networks, arXiv.

Donoho, D.L. (2006) “Compressed sensing,” IEEE Transactions on Information Theory, 52(4), pp. 1289–1306. doi:10.1109/TIT.2006.871582.

Duan, J. et al. (2019) “Vs-net: Variable splitting network for accelerated parallel MRI reconstruction,” Lecture Notes in Computer Science (including subseries Lecture Notes in Artificial Intelligence and Lecture Notes in Bioinformatics), 11767 LNCS, pp. 713–722. doi:10.1007/978-3-030-32251-9_78.

Eo, T. et al. (2018) “KIKI-net: cross-domain convolutional neural networks for reconstructing undersampled magnetic resonance images,” Magnetic Resonance in Medicine, 80(5), pp. 2188–2201. doi:10.1002/mrm.27201.

Epperson, K. et al. (2013) “Creation of Fully Sampled MR Data Repository for Compressed Sensing of the Knee,” SMRT Conference, 2013, p. 1.

Hammernik, K. et al. (2018) “Learning a variational network for reconstruction of accelerated MRI data,” *Magnetic Resonance in Medicine*, 79(6), pp. 3055–3071. doi:10.1002/mrm.26977.

Hammernik, K. et al. (2021) “Systematic evaluation of iterative deep neural networks for fast parallel MRI reconstruction with sensitivity-weighted coil combination,” *Magnetic Resonance in Medicine*, (August 2020), pp. 1859–1872. doi:10.1002/mrm.28827.

Huang, Q. et al. (2019) “MRI Reconstruction Via Cascaded Channel-Wise Attention Network,” in 2019 IEEE 16th International Symposium on Biomedical Imaging (ISBI 2019). IEEE, pp. 1622–1626. doi:10.1109/ISBI.2019.8759423.

Johnson, P.M. et al. (2021) “Evaluation of the Robustness of Learned MR Image Reconstruction to Systematic Deviations Between Training and Test Data for the Models from the fastMRI Challenge,” *Lecture Notes in Computer Science (including subseries Lecture Notes in Artificial Intelligence and Lecture Notes in Bioinformatics)*, 12964 LNCS, pp. 25–34. doi:10.1007/978-3-030-88552-6_3.

Karkalousos, D. and Caan, M. (2021) “MRI Data Consistency.” Available at: <https://github.com/wdika/mridc>.

Kingma, D.P. and Ba, J.L. (2015) “Adam: A method for stochastic optimization,” 3rd International Conference on Learning Representations, ICLR 2015 - Conference Track Proceedings, pp. 1–15.

Knoll, F. et al. (2020) “Advancing machine learning for MR image reconstruction with an open competition: Overview of the 2019 fastMRI challenge,” *Magnetic Resonance in Medicine*, 84(6), pp. 3054–3070. doi:10.1002/mrm.28338.

Li, S. et al. (2018) “Independently Recurrent Neural Network (IndRNN): Building A Longer and Deeper RNN,” *Proceedings of the IEEE Computer Society Conference on Computer Vision and Pattern Recognition*, (1), pp. 5457–5466. doi:10.1109/CVPR.2018.00572.

Lønning, K. et al. (2019) “Recurrent inference machines for reconstructing heterogeneous MRI data,” *Medical Image Analysis*, 53, pp. 64–78. doi:10.1016/j.media.2019.01.005.

Lustig, M., Donoho, D. and Pauly, J.M. (2007) “Sparse MRI: The application of compressed sensing for rapid MR imaging,” *Magnetic Resonance in Medicine*, 58(6), pp. 1182–1195. doi:10.1002/mrm.21391.

Muckley, M.J. et al. (2020) “State-of-the-Art Machine Learning MRI Reconstruction in 2020: Results of the Second fastMRI Challenge.” Available at: <http://arxiv.org/abs/2012.06318>.

Muckley, M.J. et al. (2021) “Results of the 2020 fastMRI Challenge for Machine Learning MR Image Reconstruction,” *IEEE Transactions on Medical Imaging* [Preprint]. doi:10.1109/TMI.2021.3075856.

Paszke, A. et al. (2019) “PyTorch: An Imperative Style, High-Performance Deep Learning Library,” *Advances in Neural Information Processing Systems*, 32. Available at: <https://arxiv.org/abs/1912.01703v1> (Accessed: November 23, 2021).

Penny, W. et al. (2007) *Statistical Parametric Mapping: The Analysis of Functional Brain Images*, *Statistical Parametric Mapping: The Analysis of Functional Brain Images*. Elsevier. doi:10.1016/B978-0-12-372560-8.X5000-1.

Pezzotti, N. et al. (2020) “An Adaptive Intelligence Algorithm for Undersampled Knee MRI Reconstruction,” *IEEE Access*, 8, pp. 204825–204838. doi:10.1109/ACCESS.2020.3034287.

Pruessmann, K.P. et al. (1999) “SENSE: Sensitivity encoding for fast MRI,” *Magnetic Resonance in Medicine*, 42(5), pp. 952–962. doi:10.1002/(SICI)1522-2594(199911)42:5<952::AID-MRM16>3.0.CO;2-S.

Putzky, P. et al. (2019) “i-RIM applied to the fastMRI challenge,” *arXiv* [Preprint].

Putzky, P. and Welling, M. (2017) “Recurrent Inference Machines for Solving Inverse Problems,” *arXiv* [Preprint], (Nips). Available at: <http://arxiv.org/abs/1706.04008>.

Quan, T.M., Nguyen-Duc, T. and Jeong, W.K. (2018) “Compressed Sensing MRI Reconstruction Using a Generative Adversarial Network With a Cyclic Loss,” *IEEE Transactions on Medical Imaging*, 37(6), pp. 1488–1497. doi:10.1109/TMI.2018.2820120.

Ramzi, Z., Ciuciu, P. and Starck, J.L. (2020) “Benchmarking Deep Nets MRI Reconstruction Models on the Fastmri Publicly Available Dataset,” *Proceedings - International Symposium on Biomedical Imaging*, 2020-April, pp. 1441–1445. doi:10.1109/ISBI45749.2020.9098335.

Ramzi, Z., Ciuciu, P. and Starck, J.-L. (2020) “XPDNet for MRI Reconstruction: an Application to the fastMRI 2020 Brain Challenge,” *arXiv* [Preprint]. doi:10.1100/mrm.21391.

Ronneberger, O., Fischer, P. and Brox, T. (2015) “U-net: Convolutional networks for biomedical image segmentation,” *Lecture Notes in Computer Science (including subseries Lecture Notes in Artificial Intelligence and Lecture Notes in Bioinformatics)*, 9351, pp. 234–241. doi:10.1007/978-3-319-24574-4_28.

Sarroff, A.M., Shepardson, V. and Casey, M.A. (2015) “Learning Representations Using Complex-Valued Nets.” Available at: <http://arxiv.org/abs/1511.06351> (Accessed: August 10, 2021).

Schlemper, J. et al. (2018) “A Deep Cascade of Convolutional Neural Networks for Dynamic MR Image Reconstruction,” *IEEE Transactions on Medical Imaging*, 37(2), pp. 491–503. doi:10.1109/TMI.2017.2760978.

Schlemper, J. et al. (2019) “\$\Sigma\$-net: Ensembled Iterative Deep Neural Networks for Accelerated Parallel MR Image Reconstruction.” Available at: <https://arxiv.org/abs/1912.05480v1> (Accessed: July 28, 2021).

Sodickson, D.K. and Manning, W.J. (1997) “Simultaneous acquisition of spatial harmonics (SMASH): Fast imaging with radiofrequency coil arrays,” *Magnetic Resonance in Medicine*, 38(4), pp. 591–603. doi:10.1002/mrm.1910380414.

Souza, R. et al. (2019) “A Hybrid, Dual Domain, Cascade of Convolutional Neural Networks for Magnetic Resonance Image Reconstruction,” Proceedings of Machine Learning Research 102:437–446, 102, pp. 1–11.

Souza, R. et al. (2020) “Dual-domain cascade of U-nets for multi-channel magnetic resonance image reconstruction,” Magnetic Resonance Imaging, 71, pp. 140–153. doi:10.1016/J.MRI.2020.06.002.

Sriram, A., Zbontar, J., Murrell, T., Defazio, A., et al. (2020) “End-to-End Variational Networks for Accelerated MRI Reconstruction,” Lecture Notes in Computer Science (including subseries Lecture Notes in Artificial Intelligence and Lecture Notes in Bioinformatics), 12262 LNCS, pp. 64–73. doi:10.1007/978-3-030-59713-9_7.

Sriram, A., Zbontar, J., Murrell, T., Zitnick, C.L., et al. (2020) “GrappaNet: Combining Parallel Imaging with Deep Learning for Multi-Coil MRI Reconstruction,” Proceedings of the IEEE Computer Society Conference on Computer Vision and Pattern Recognition, pp. 14303–14310. doi:10.1109/CVPR42600.2020.01432.

Strijbis, V.I.J. et al. (2021) “Multi-view convolutional neural networks for automated ocular structure and tumor segmentation in retinoblastoma,” Scientific Reports, 11(1), p. 14590. doi:10.1038/s41598-021-93905-2.

Uecker, M. et al. (2014) “ESPIRiT—an eigenvalue approach to autocalibrating parallel MRI: Where SENSE meets GRAPPA,” Magnetic Resonance in Medicine, 71(3), pp. 990–1001. doi:10.1002/mrm.24751.

Uecker, M. et al. (2015) “Berkeley Advanced Reconstruction Toolbox,” Proc. Intl. Soc. Mag. Reson. Med., 23.

Wang, K. et al. (no date) Memory-efficient Learning for High-Dimensional MRI Reconstruction.

Wang, S. et al. (2020) “DeepcomplexMRI: Exploiting deep residual network for fast parallel MR imaging with complex convolution,” Magnetic Resonance Imaging, 68(February), pp. 136–147. doi:10.1016/j.mri.2020.02.002.

Wang, Z. et al. (2004) “Image quality assessment: From error visibility to structural similarity,” IEEE Transactions on Image Processing, 13(4), pp. 600–612. doi:10.1109/TIP.2003.819861.

Yang, G. et al. (2018) “DAGAN: Deep De-Aliasing Generative Adversarial Networks for Fast Compressed Sensing MRI Reconstruction,” IEEE Transactions on Medical Imaging, 37(6), pp. 1310–1321. doi:10.1109/TMI.2017.2785879.

Yang, Y. et al. (2017) “ADMM-net: A deep learning approach for compressive sensing MRI,” arXiv, pp. 1–14.

Zbontar, J. et al. (2018) “fastMRI: An open dataset and benchmarks for accelerated MRI,” arXiv, pp. 1–35.

Zhang, H. and Mandic, D.P. (2016) “Is a complex-valued stepsize advantageous in complex-valued gradient learning algorithms?,” IEEE Transactions on Neural Networks and Learning Systems, 27(12), pp. 2730–2735. doi:10.1109/TNNLS.2015.2494361.

Zhang, X. et al. (2020) “A deep unrolling network inspired by total variation for compressed sensing MRI,” Digital Signal Processing: A Review Journal, 107, p. 102856. doi:10.1016/j.dsp.2020.102856.

Zhao, R. et al. (2021) “fastMRI+: Clinical Pathology Annotations for Knee and Brain Fully Sampled Multi-Coil MRI Data,” pp. 1–7. Available at: <http://arxiv.org/abs/2109.03812>.

Zhu, B. et al. (2018) “Image reconstruction by domain-transform manifold learning,” Nature, 555(7697), pp. 487–492. doi:10.1038/nature25988.

Appendix

Gated Recurrent Unit (GRU)

The GRU has two gating units, the reset gate and the update gate. These gates control how the information flows in the network. The update gate regulates the update to a new hidden state, whereas the reset gate controls the information to forget. Both gates act in a probabilistic manner.

The activation of the reset gate r at time-step τ , for updating (13), is computed by

$$r_\tau = \sigma(W_r[s_{\tau-1}, x_\tau] + b_r).$$

σ is the logistic sigmoid function, x_τ and $s_{\tau-1}$ are the input and the previous hidden state, respectively. W_r and b_r are the weights matrix and the learned bias vector.

Similarly, the update gate z is computed by

$$z_\tau = \sigma(W_z[s_{\tau-1}, x_\tau] + b_z).$$

The actual activation of the next hidden state s_τ is then computed by

$$s_\tau = (1 - z_\tau) \odot s_{\tau-1} + z_\tau \odot \tilde{s}_\tau,$$

where \odot represents the Hadamard product and \tilde{s}_τ is given by

$$\tilde{s}_\tau = \tanh(W_s[r_\tau \odot s_{\tau-1}, x_\tau] + b_s).$$

Independently Recurrent Neural Network

The IndRNN addresses gradient decay over iterations, following an independent neuron connectivity within a recurrent layer. The update at time-step τ can be described as

$$s_\tau = \sigma(Wx_\tau + u \odot s_{\tau-1} + b),$$

where W is the weight for the current input, u is the weight for the recurrent input, and b is the bias.

Supplementary

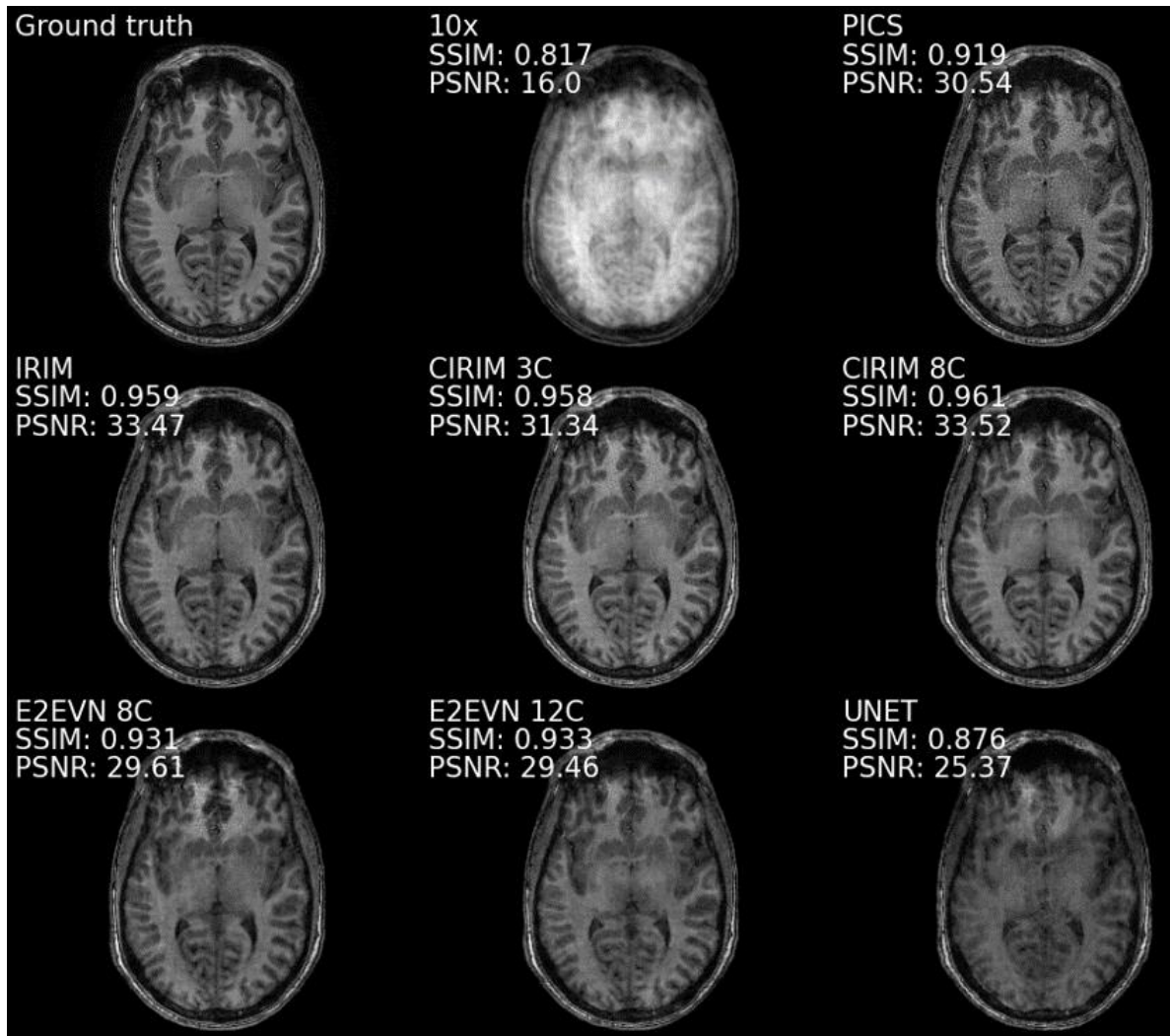


Figure S1: Reconstructions of a ten times accelerated slice from the T_1 -weighted brains dataset (first row-second). The ground truth is presented on the first row-first image. The IRIM (second row-first), the CIRIM 3C (second row-second), and the CIRIM 8C (second row-third) enforced Data Consistency (DC) implicitly by gradient descent. The E2EVN 8C (third row-first) and the E2EVN 12C (third row-second) enforced DC explicitly by a formulated DC term.

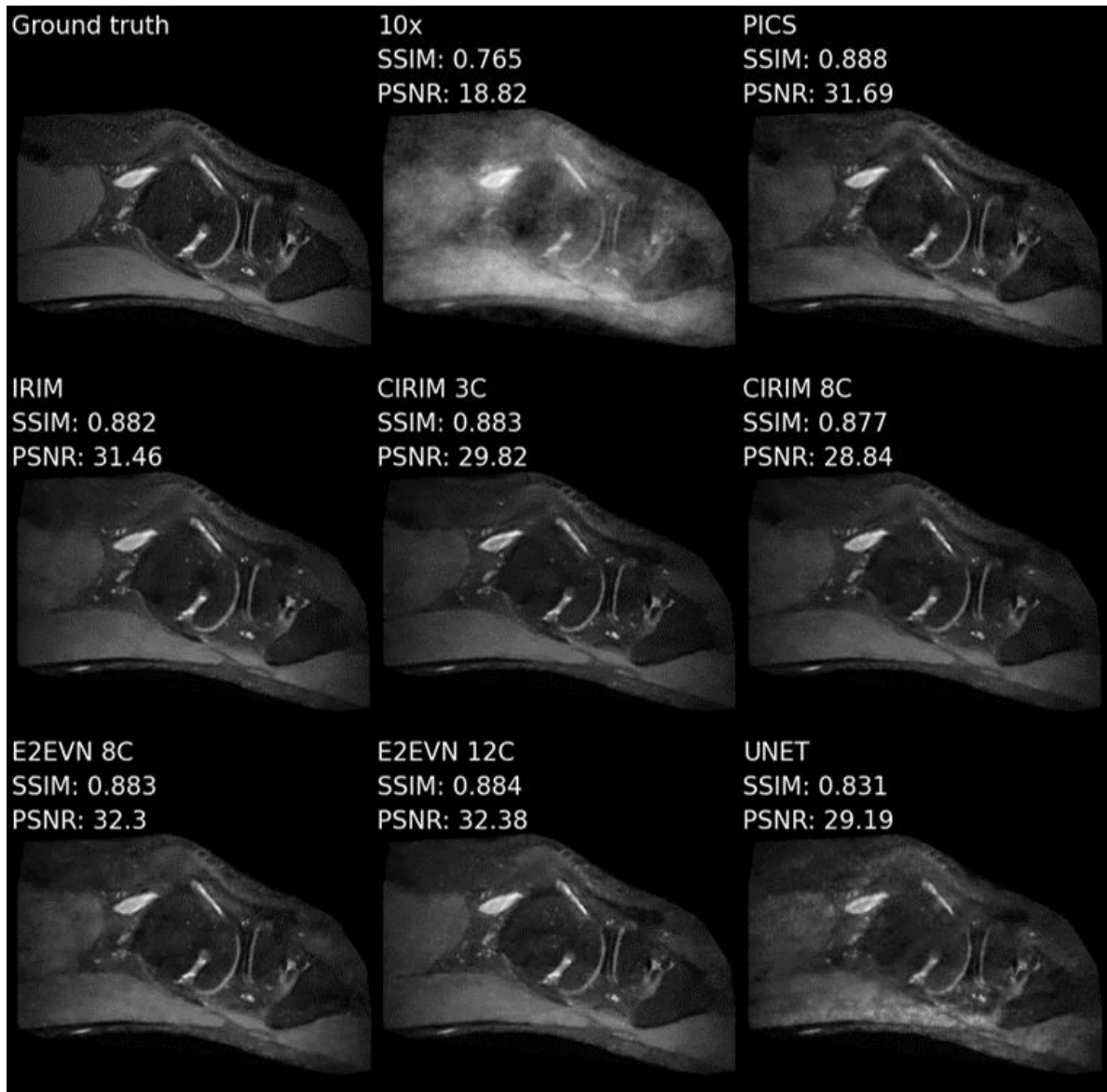


Figure S2: Reconstructions of a ten times accelerated slice from the T_2 -weighted knees dataset (first row-second). The ground truth is presented on the first row-first image. The IRIM (second row-first), the CIRIM 3C (second row-second), and the CIRIM 8C (second row-third) enforced Data Consistency (DC) implicitly by gradient descent. The E2EVN 8C (third row-first) and the E2EVN 12C (third row-second) enforced DC explicitly by a formulated DC term.

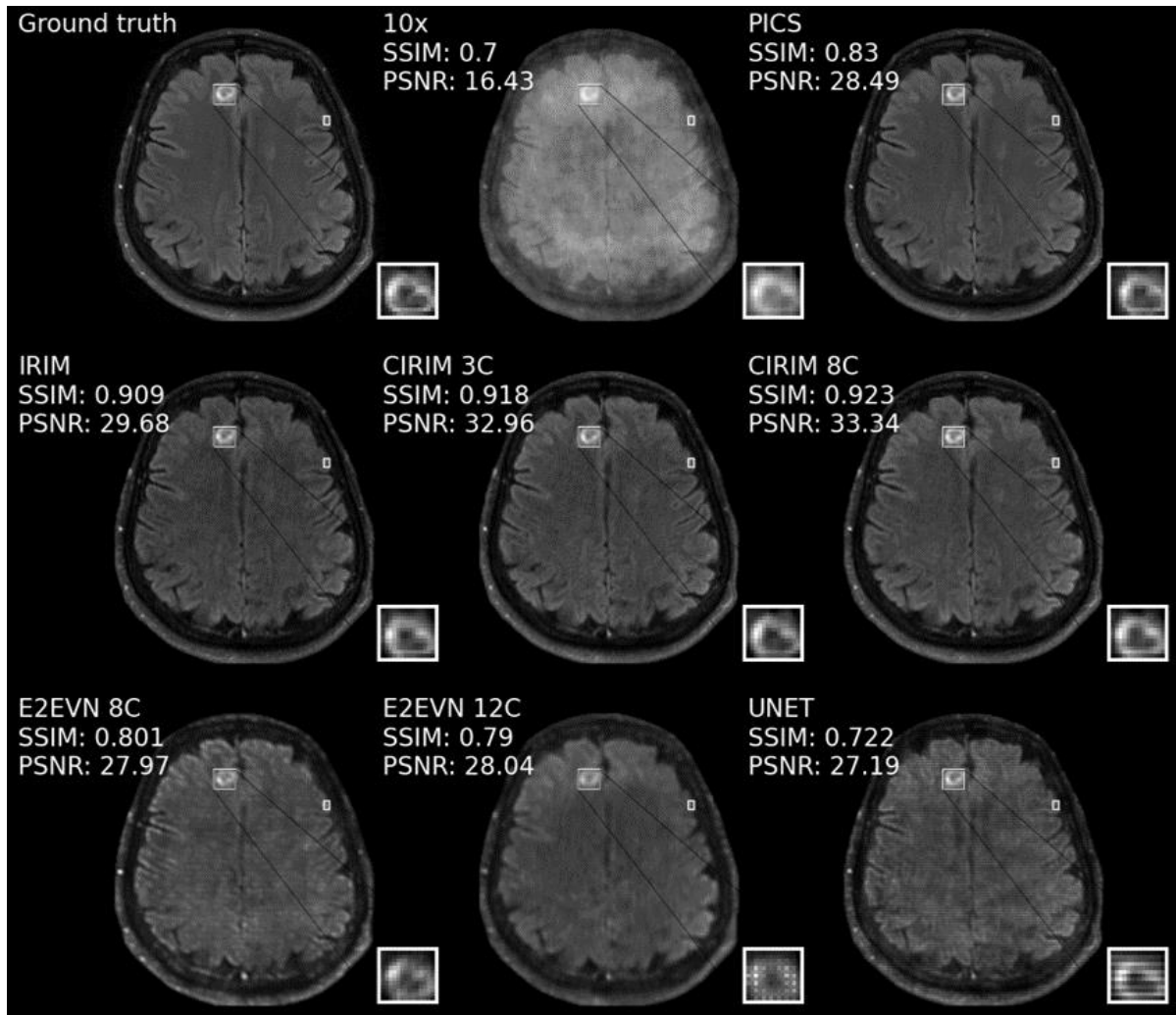


Figure S3: Reconstructions of a ten times accelerated slice from the FLAIR brains dataset (first row-second). The ground truth is presented on the first row-first image. The inset focuses on a reconstructed White Matter lesion; obtained through the fastMRI+ annotations (Zhao et al., 2021). The IRIM (second row-first), the CIRIM 3C (second row-second), and the CIRIM 8C (second row-third) enforced Data Consistency (DC) implicitly by gradient descent. The E2EVN 8C (third row-first) and the E2EVN 12C (third row-second) enforced DC explicitly by a formulated DC term.